The Role of Microstructure Morphology on Fracture Mechanisms of Continuously Cooled Bainitic Steel Designed for Rails Application

ALEKSANDRA KRÓLICKA, GRZEGORZ LESIUK, ROMAN KUZIAK, KRZYSZTOF RADWAŃSKI, and ALEKSANDRA JANIK

The low-carbon bainitic steel after a continuous cooling process was subjected to fracture toughness investigations using the J-integral approach. The research was focused on the determination of microstructural factors influencing the fracture processes considering the crystallographic units, as well as dimensions and morphology of phases. It was found that the fracture surface is characterized by complex fracture mechanisms (quasi-cleavage, transcrystalline cleavage–ductile, and ductile mode). It was found that the main features influencing the cracking processes are bainitic ferrite packets and prior austenite grain boundaries. The changes in the crack path were also related to the changes in the misorientation angles, and it was found that changes in the crack path direction occur mainly for the bainitic ferrite packets (HABs). Also, the fracture process zone induced by the crack tip was identified. At a distance of about 4 to 5 μm from the fracture, the retained blocky austenite transformed into martensite was observed. Due to the high carbon content in the retained austenite, the transformed martensite was brittle and was the site of microcracks nucleation. Another origin of microcracks nucleation were M/A constituents occurred in the initial microstructure. In the crack tip area, the reduced dislocation density in the bainitic ferrite, which was caused by the formation of sub-grains, was also determined. Finally, the prospective improvement of the fracture toughness of bainitic steels was determined.

I. INTRODUCTION

IT is well reported in the literature that bainitic steels are the major competitors for pearlitic steels in terms of rail infrastructure applications. Generally, steels used for infrastructure applications should exhibit the demanding requirements regarding their mechanical properties and performance in service. High-strength carbide-free bainitic steels are particularly promising due to their fatigue behavior and mechanical properties.[1] Based on the majority of published investigations, one may conclude that bainitic rails are characterized by significantly higher static tensile strength, wear resistance, toughness, and fatigue performance than conventional pearlitic rails.[2–7] Generally, the designed bainitic steel grades are subjected to low-temperature isothermal transformation treatment (so-called by some authors as bainitization) to maximize the bainite fraction and obtain retained austenite films[1,3,8] separating bainitic ferrite laths. In terms of industrialization, the need for additional heat treatment generates higher manufacturing costs especially as the process may be lengthy due to the long times required at the bainitization stage. However, Gao et al. proposed a method intended for the acceleration of the bainitic transformation during isothermal heat treatment of bainitic rail steels by pre-existing bainite.[9] In recent years, apart from bainitic steels requiring isothermal heat treatment, continuously cooled low-carbon bainitic steels (below 0.3 wt pct C) that do not require additional heat treatment were also investigated in the literature.[10–16] Generally, these steels are characterized by sub-micrometric dimensions (100 ÷ 1000 nm) of the structure

ALEKSANDRA KRÓLICKA is with the Department of Metal Forming, Welding and Metrology, Faculty of Mechanical Engineering, Wroclaw University of Science and Technology, Wybrzeże Wyspiańskiego 27, 50-370, Wroclaw, Poland. GRZEGORZ LESIUK is with the Department of Mechanics, Materials and Biomedical Engineering, Faculty of Mechanical Engineering, Wroclaw University of Science and Technology, Wybrzeże Wyspiańskiego 27, 50-370, Wroclaw, Poland. ROMAN KUZIAK, KRZYSZTOF RADWAŃSKI, and ALEKSANDRA JANIK are with the Łukasiewicz Research Network-Institute for Ferrous Metallurgy, K. Miarki 12-14, 44-100, Gliwice, Poland. Contact e-mail: aleksandra.krolicka@pwr.edu.pl
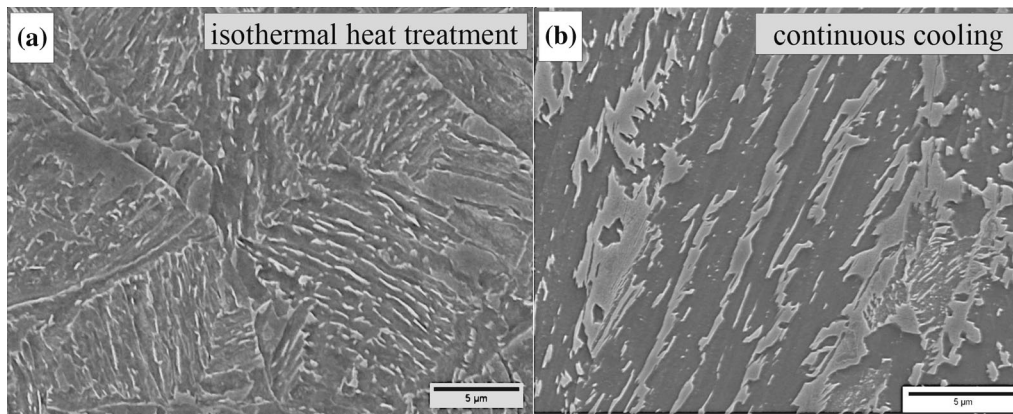
Fig. 1—Comparison of the microstructure of the tested steel: (*a*) isothermal heat treatment at 360 °C for 2 h, (*b*) continuous cooling processes.

constituents, namely, the thickness of the bainitic ferrite laths and the filmy austenite.[10,16] These also contain the so-called blocky retained austenite, and due to its low thermal stability, it may be fully or partially transformed into martensite during continuous cooling, forming M/A islands.[10] Also, Adamczyk-Cieślak et al.[17] compared the mechanical properties of bainitic steel rails after isothermal heat treatment and continuous cooling processes. It was found that low-carbon steel after a continuous cooling process is characterized by a more favorable combination of strength and elongation compared to the isothermally heat treatment process.

Based on current investigations and published results,[18–21] the scheme characterizing the effect of continuous cooling and isothermal heat treatment on the microstructure of bainitic steels was developed (Figure 1). Generally, during the bainitic transformation the prior austenite grain (PAG) may be divided into packets with a similar habit plane with respect to austenite. Each packet contains blocks and retained austenite. Moreover, each block contains the filmy retained austenite film and the bainitic ferrite laths.[20] Also, a sub-block and a single variant of laths may be formed.[22] Thus, the smallest crystallographic unit is the bainitic ferrite lath. However, it should be emphasized that the fraction of phases in bainitic steels is significantly different after continuous cooling processes compared to isothermal heat treatment. The major difference is related to the stability of the retained austenite and the formation of the M/A constituents, which appear between the bainitic ferrite laths and at the boundaries of the prior austenite grain (Figures 1, 2). Figure 1 contains a comparison of the continuous cooling process and isothermal heat treatment of the tested steel. These differences are summarized in a scheme that also includes the crystallographic units (Figure 2).

It is well known that the structure morphology directly influences the mechanical properties of bainitic steels. In the context of multi-phase structures, the fracture processes may vary significantly depending on the fraction, chemical composition, degree of refinement, and distribution of the obtained phases. It was
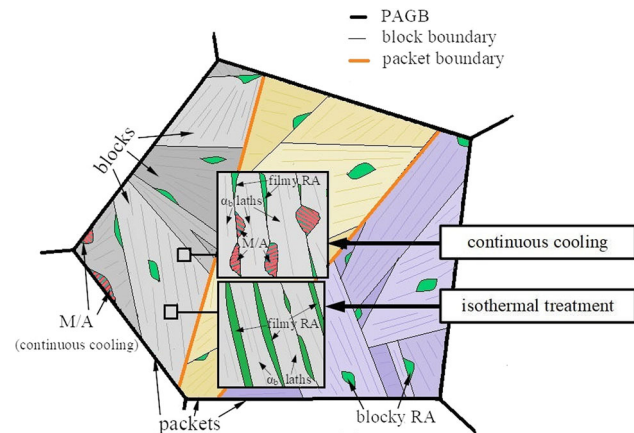

Fig. 2—Scheme of bainite morphology developed inside prior austenite grain formed during continuous cooling and isothermal heat treatment of low-carbon steels. *RA* retained austenite, *M/A* martensite/austenite constituents, *PAGB* prior austenite grain boundary, α*b* bainitic ferrite.

found that the lath morphology of bainitic ferrite is characterized by significantly higher impact toughness compared to granular morphology.[23] In many investigations, it was stated that M/A constituents are the favorable site for crack nucleation and damage initiation.[13,24] Also, coarse retained blocky austenite during fracture transforms to martensite, preferentially in areas of low-carbon concentrations.[24] Another structural feature that may be connected to the crack nucleation process is the occurrence of coarse carbide or carbides colonies.[25] On the other hand, filmy austenite is a feature that positively influences the fracture process and hinders crack propagation.[24,26–31] It was also found that packets are responsible for significant changes in the crack path, while the close-packet boundaries inside the packets and M/A constituents influence the local changes of the crack path.[19] Generally, the packet boundaries are characterized by high-angle misorientation boundaries (HABs) near the 48 and 55 deg, while block boundaries are characterized by the lower misorientation angle.[32] Moreover, refined prior austenite grains enhance the fraction of HABs in the entire microstructure, which results in toughness

improvement.[33,34] Therefore, apart from morphology and phase fraction, crystallographic units (blocks, packets) also play a crucial role in the fracture toughness of bainitic steels.[35]

An important measure of fracture toughness is the determination of critical stress intensity factor values or other parameters based on non-linear fracture mechanics, such as CTOD (Crack Tip Opening Displacement) or the elastic–plastic J integral. The present research is focused on explaining the effect of the crack tip propagation on the evolution of the microstructure of continuously cooled bainite steel and on determining the role of the microstructure on the fracture process. This is an essential part of elastic–plastic fracture testing.

The present research is focused on explaining the impact of the crack tip on the evolution of the microstructure of continuously cooled bainite steel. The multi-phase structure of the test steel is described in detail qualitatively and quantitatively and then compared to the fracture process zone. The influence of crystallographic features of (bainitic ferrite packets and blocks), martensite transformation of the retained austenite, and dislocation density are considered. The obtained results allow for the development of cracking process scenarios for continuously cooled low-carbon bainitic steels and indicate the prospects for the improvement of fracture toughness.

II. MATERIALS AND METHODS

A. Materials

The production technology of the bainitic rail was developed by Łukasiewicz Research Network Institute—Institute for Ferrous Metallurgy (Gliwice, Poland) in cooperation with ArcelorMittal Poland. Moreover, this grade was also analyzed after the service.[36] The chemical composition of the tested steel was designed towards obtaining bainitic structure after natural continuous cooling in still air directly after hot rolling (without the additional isothermal heat treatment). Due to the differential cooling rates occurring during the manufacturing process related to the dimensions of the 60E1 rail, structural differences in cross section are also expected. In order to avoid the potential impact of structure changes at the rail surface, it was decided to analyze the rail head core, where the lowest cooling rates were observed. In this area, the structure was characterized by a homogeneous structure and comparable hardness. All provided data are also consistent with the core of the rails head. Thus, it is necessary to emphasize the importance of the complexity of structures after continuous cooling, where it is difficult to obtain a homogeneous structure in the area of the entire cross section. Subsequent research should also focus on comparing the material properties in the core and at the surface or neck of the rail, where higher cooling rates occurred. A general concept of the chemical composition of the tested material is presented

Table I. Chemical Composition Concept of Tested Continuously Cooled Bainitic Steel

Chemical Composition [Wt Pct]						
C	Mn	Cr	Si	Ni	Mo	Fe
~ 0.3	2.5 (Mn + Cr)		Min. 0.8	low content		balance

Table II. Mechanical Properties of Rails Tested in this Research

UTS [MPa]	$\sigma_{pl}/\sigma_{0.2}$ [MPa]	YR	A_5 [Pct]	HV10
Min. 1250	Min 700	0.56–0.68	Min. 17.0	Min. 408

UTS—Ultimate tensile strength, $\sigma_{pl}/\sigma_{0.2}$—yield stress, YR—yield ratio, HV10—Vickers hardness with a load of 98.1 N.

in Table I. Due to the imposed regulations, the precise chemical composition of the analyzed alloy is not presented. The tested bainitic rail contains an increased content of Si, Cr, and Mn (also low content of Ni and Mo). Chromium and manganese effectively improve the hardenability and contribute to solid solution strengthening. Additionally, relatively high silicon content suppresses the iron carbides precipitation process from austenite.[37,38] The mechanical properties of bainitic rails are presented in Table II. Ultimate tensile strength of 1275 MPa and yield stress of 780 MPa classify tested steel as high-strength material. It should also be mentioned that the tested material was also the subject of previous research in the context of the welding processes[39,40] and fatigue crack growth rate.[16]

B. Fracture Toughness Determination

Fracture toughness tests were performed using SENB (Single Edge Notched Bend) specimen. The rail head was tested in this investigation. Specimen shape and its geometry related to the orientation of the rail are shown in Figure 3. All specimens were prepared in accordance with ASTM E1820.[41] The thickness of the specimen was 10 mm. The notch was prepared using EDM (Electro Discharging Machine) up to length $c_0 = 8.7$ mm. To provide a sharp crack tip, all specimens were pre-cracked using sinusoidal waveform ($R = 0.1$, $f = 5$ Hz) up to initial normalized crack length $c/W = 0.5$–0.52. During precracking phase maximal value of Stress Intensity Factor (SIF), K_{max} did not exceed 14–15 MPa√m. The measurement stand is shown in Figure 4.

$$\frac{P_{max}}{P_Q} \leq 1.1 \qquad [1]$$

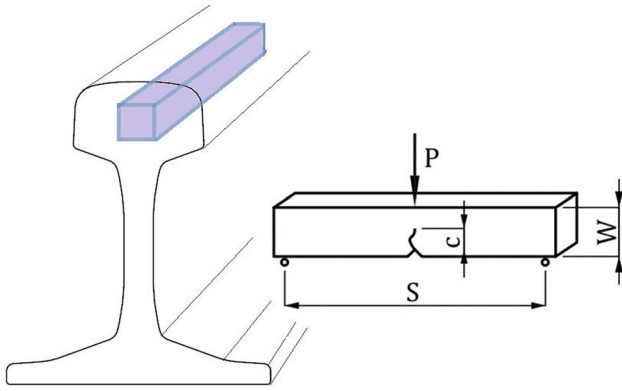SIF was calculated using following [ASTM E1820] formula:

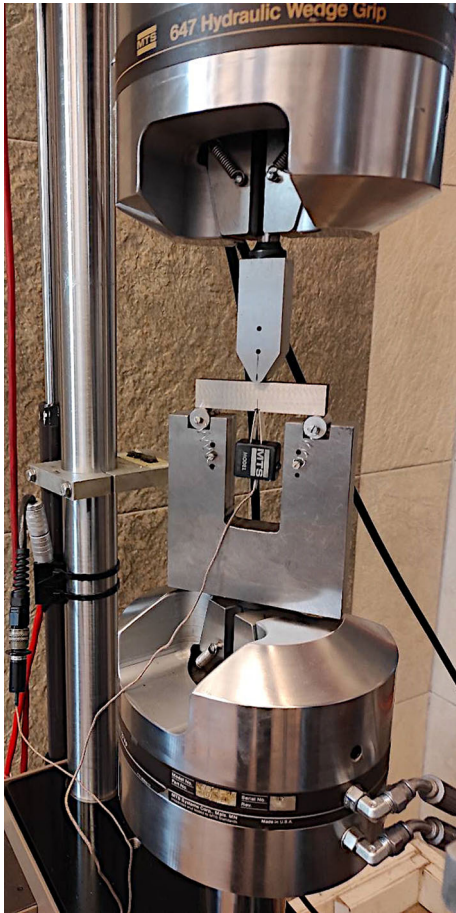Fig. 3—SENB specimen model in its dimensions; W = 20 mm, S = 800, c/W = 0.5–0.52.

Fig. 4—SENB specimen during test.

$$K_I = \frac{P_Q}{BW^{1/2}} \frac{(2 + A_w)\left[0.886 + 4.64 A_w - 13.32 A_w^2 + 14.72 A_w^3 - 5.6 A_w^4\right]}{(1 - A_w)^{3/2}},$$

[2]

where P_Q is a value of the load determined by the experiment; A_w is normalized crack length (c/W); W is width of the specimen; B is thickness of the sample after the test plane strain condition was validated to

satisfy requirements of the material data constant called as fracture toughness K_{IC}. Based on ASTM E1820[41] standard it can be calculated as

$$B, c, (W - c) > 2.5 \left(\frac{K_Q}{\sigma_\gamma}\right)^2.$$

[3]

In Eq. [3] σ_y represents the flow stress of the material.

C. Microstructure Analysis

Fractographic investigation was carried out both on the macroscale and microscale using the FEI Inspect F Scanning Electron Microscope (SEM). The fracture topography was observed immediately after the fracture toughness investigations. SEM observations were performed using secondary electrons detector (topographic contrast) and an accelerating voltage of 15 kV. The working distance was approx. 10 mm.

The microstructure observations of the bainitic rails after fracture toughness investigations were performed using a high-resolution JOEL JSM-7200F scanning electron microscope after etching by 5 pct nital. A working distance of 15 mm and an accelerating voltage of 15 kV were used. Observations of base materials microstructure were also carried out using the HITA-CHI H-800 transmission electron microscope. Samples preparation included mechanical pre-thinning of 1.0 mm plates to a thickness of approximately 80–100 μm. Then, discs with a diameter of ø3 mm were cut out by mechanical methods from the thinned plates. Subsequently, electrochemical polishing was carried out using the 10 Pct perchloric acid in butoxyethanol at 10 °C and the Struers TenuPol device. Ultimately, to improve the quality of structure observations ion polishing was performed using the GATAN DuoMill device.

The samples intended for the microstructure analysis in the fracture area were performed on the cross section. The fracture was stopped to observe the path and the crack tip in terms of evaluating the influence of microstructure morphology. The crack path was observed in the sample core. The samples after stopped fracture were immersed in an epoxy resin and then carefully ground (by sandpaper with a number of 320–1000) and polished (by a diamond medium with a size of 1 μm). Samples intended for EBSD investigations were polished using Active Oxide Polishing Suspensions (OP-A; acidic alumina suspension, the process lasted 5 min) and then were ion polished using the Fischione SEM Mill device during 3 h. The assessment of microstructure morphology on crack propagation was carried out using high-resolution scanning electron microscopy JEOM JSM-7100F equipped with Electron Back-Scattered Diffraction (EBSD) detector (EDAX). The EBSD studies were made on surface areas in the range of 2.739×10^2 to 1.545×10^4 μm^2 with a step size in the range of 40 nm to 0.47 μm. The post-processing of obtained data was carried out by applying the OIM TSL software. A single iteration grain dilation clean-up and confidence index standardization procedures were

made for each analysis. The grain size data were determined using a grain tolerance angle of 5 deg. The minimum grain size was adjusted to 2 pixels. The clean-up procedure did not exceed 5 pct of the measurement pixels.

The dislocation density in the base material and crack area was determined using Williamson–Hall[42] and Williamson–Smallman methods.[43] The analysis was performed using X-ray Empyrean (PANalytical) diffractometer with filtered CoKα (λ = 0.179 nm) radiation. The voltage of 30 kV, current of 40 mA, the angular range of 2θ from 45 to 107 deg, measurement step $\Delta 2\theta$ of 0.026, and counting time per step of 1 s were applied. The measurement area covered 50 μm and was located near the crack tip. The area in the base material was analyzed for comparative purposes. The lattice strain (ε) resulting from peak broadening was calculated by Williamson–Hall equations considering the (110), (200), and (211) ferrite planes. The lattice strain was calculated to determine the dislocation density (ρ) using the following equation described by Williamson and Smallman[43]

$$\rho = k\frac{\varepsilon^2}{b^2}, \qquad [4]$$

where k is a constant value and b is the magnitude of the Burgers vector. It was assumed that the magnitude of Burgers vector is $b = a/2$. The k value for the calculation of the bcc system is 14.4.[44] The dislocation density calculations for austenite were not performed due to its negligible fraction in the crack area. Crystallite size was calculated using the Scherrer equation:

$$D = K\alpha/\beta\cos\theta, \qquad [5]$$

where D is the average crystallite size, K is a Scherrer constant, α is the X-ray wavelength, β is the line broadening at FWHM, and θ is the Bragg's angle.

The X-Ray diffraction analysis (XRD) was performed to measure the phase constituents volume fraction of experimental material. The obtained data were also applied to determine the carbon concentration in retained austenite using equation described by Dyson and Holmes[45]:

$$\begin{aligned} a_\gamma = &\ 3.578 + 0.033w_{C\gamma} + 0.00095w_{Mn} - 0.0002w_{Ni} \\ &+ 0.0006w_{Cr} + 0.022w_N + 0.0056w_{Al} \\ &- 0.0004w_{Co} + 0.0015w_{Cu} + 0.0031w_{Mo} \\ &+ 0.0051w_{Nb} + 0.0039w_{Ti} + 0.0018w_V + 0.0018w_W, \end{aligned}$$
$$[6]$$

where w indicates the wt pct of given chemical elements and a_γ measured lattice parameter based on XRD data considering (111), (200), (220), and (311) diffraction peaks. The analysis was performed using X-ray Empyrean (PANalytical) diffractometer with filtered CoKα (λ = 0.179 nm) radiation. The voltage of 30 kV, current of 40 mA, the angular range of 2θ from 45 to 110 deg, measurement step $\Delta 2\theta$ of 0.026, and counting time per step of 1 s were applied. The quantitative analysis was carried out by the Rietveld method.

Nanoindentation was carried out using Anton Paar, NHT3 equipment with a Berkovich-type tip, calibrated on fused silica samples. The load of 10 mN and the dwell time of 30 s was applied. The unloading and loading rates were 20 mN/min. The hardness a were calculated using the Oliver and Pharr method similar to work.[46] A hardness map was made in an area with dimensions of approx. 26×33 μm, where 49 measurements were carried out. The distances between the indentations were in the range of 3.5–5.0 μm.

III. RESULTS AND DISCUSSION

A. Fracture Toughness

Typical F-CMOD diagrams are presented in Figure 5. Based on the presented plots, it should be noted that both specimens exhibit low ductility levels, which may affect linear elastic fracture mechanics (LEFM) validity for plane strain conditions (Eq. [3]).

To investigate controlled elastic–plastic fracture, one specimen was loaded typically as for J-integral test with unloading level to evaluate incremental crack growth and arresting during the experiment for further materials' investigation of the microstructure in the vicinity of a crack tip. Typical load F-CMOD dependence is shown in Figure 6.

For the tested bainitic rail steel, the average critical stress intensity factor K_Q is equal to 58.9 MPa$\sqrt{m}$. The obtained value is significantly higher, as for reported values of fracture resistance for pearlitic steel. Particularly noteworthy is its closer value to the ones reported in papers[4,6,48,49] for bainitic steel. It confirms a higher ductility level of bainitic rail steel compared to pearlitic steel.

B. Microstructure Morphology After Natural Continuous Cooling

The microstructure of bainitic rails after natural continuous cooling is presented in Figures 7 and 8. A lath-like bainitic ferrite morphology was found, which also contained M/A constituents and a negligible
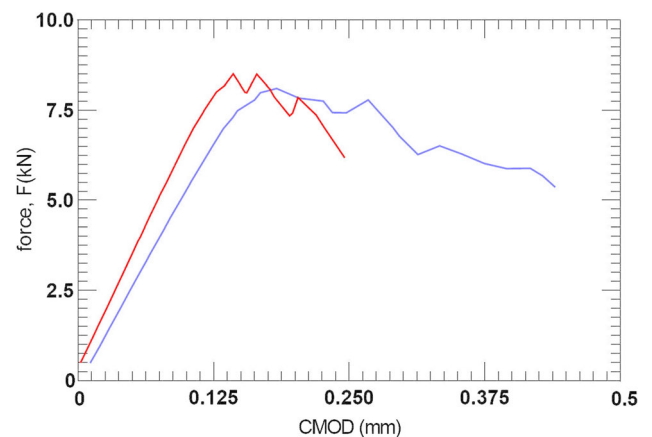

Fig. 5—Force–CMOD curves for samples 1 and 2.

fraction of carbide precipitates in the bainitic ferrite (Figure 7). Both morphologies (filmy and blocky) of the retained austenite were also identified. Nanometric filmy austenite was also observed is presented in the

Fig. 6—Force–CMOD curves for specimen 3 with unloading steps. Based on the experimental analysis, all results are collected in Table III.

bright-field image obtained using transmission electron microscopy (TEM) method—Figures 8(a) and Figure 8b. The areas of the M/A islands were also found [Figure 8(c)], which indicates insufficient thermal stability of austenite during cooling. In general, the refinement degree of the structure can be evaluated as sub-micrometric, and the thickness range of the bainitic ferrite laths was in the range of 150 to 450 nm when the filmy austenite was in the range of 80 to 200 nm. On the other hand, the median from prior austenite grains size was determined as 47 μm.[39]

To quantify the structure components, XRD measurements were performed, and the carbon concentration in the residual austenite was determined. The results were related to the determined temperature T_0', calculated using mucg83.[50] The temperatures T_0 are important in terms of evaluating the diffusionless growth, which can only occur if the austenite carbon concentration ($C\gamma$) does not exceed the determined curve.[51] The points on the T_0 curve designate carbon concentrations, where ferrite and austenite with the same chemical composition exhibit the same free energy.[38,52] On the other hand, the T_0' is defined similarly to T_0 but considering the stored energy of the bainitic ferrite (400 Jmol^{-1}) due to the displacive mechanism of bainite

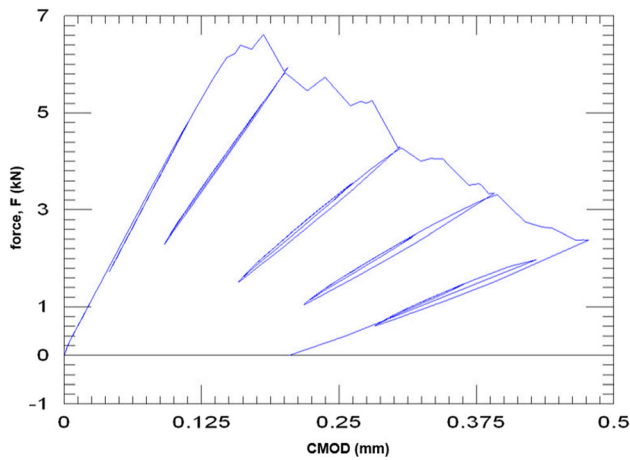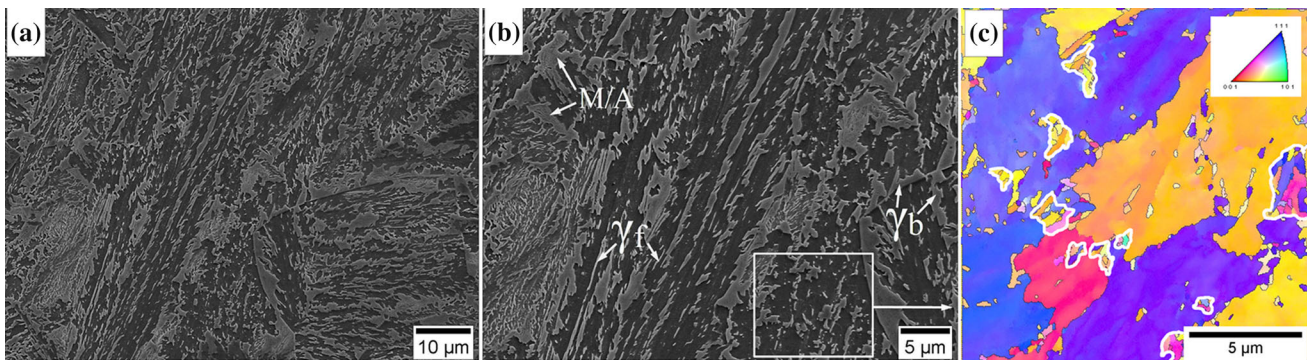Fig. 7—(a) The microstructure of continuously cooled bainitic rail. (b) Magnified area of bainitic ferrite, filmy retained austenite (γ_f), blocky retained austenite (γ_b), and M/A islands. SEM, SE detector, (c) Inverse Pole Figure Map of the selected area indicated in the frame. Analysis area 16 μm × 16 μm, step size 40 nm.
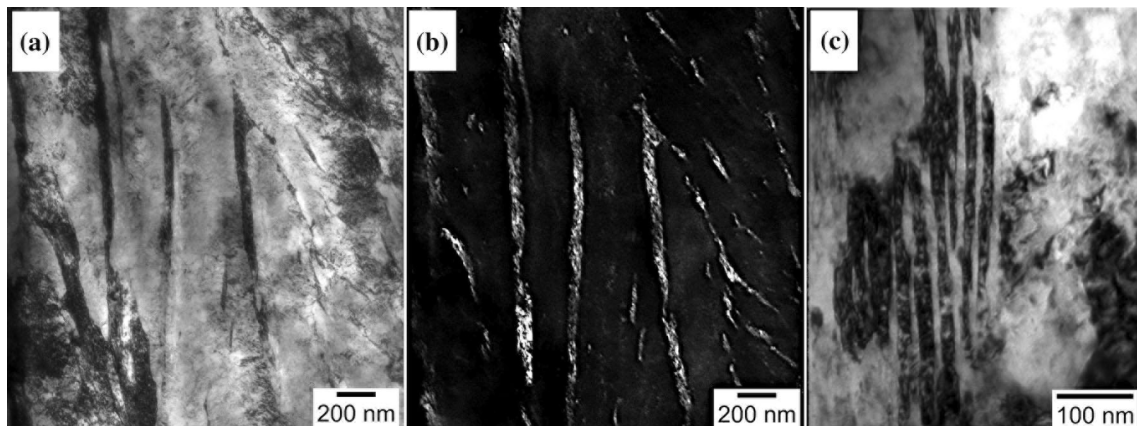

Fig. 8—The microstructure of continuously cooled bainitic rail. (a) Bright-field image of bainitic ferrite laths and filmy retained austenite: $[001]_\alpha \| [01\bar{1}]_\gamma$. (b) Dark-field image from austenite diffraction reflex. (c) Area of densely populated M/A constituents. TEM, 150 kV.

Table III. Fracture Toughness Test Results

	#1	#2	#3	Pearlitic rail Steel	Bainitic Rail Steel
P_{max} (kN)	8.1	8.5	6.6	n/a	n/a
Initial Crack Length c/W	0.51	0.48	0.55	n/a	n/a
K_Q (MPa√m)	60.4	57.6	58.7	32.5[47]	95[6]*
				41[6]	52[48]
				41[48]	51.6[4]
				41.7[4]	
$P_{max}/P_Q < 1.1$	Yes	Yes	Yes	n/a	n/a

*non-standard specimen used for the test, initially normalized crack length $c/W = 0.36$ was significantly lower than in normalized fracture toughness test.
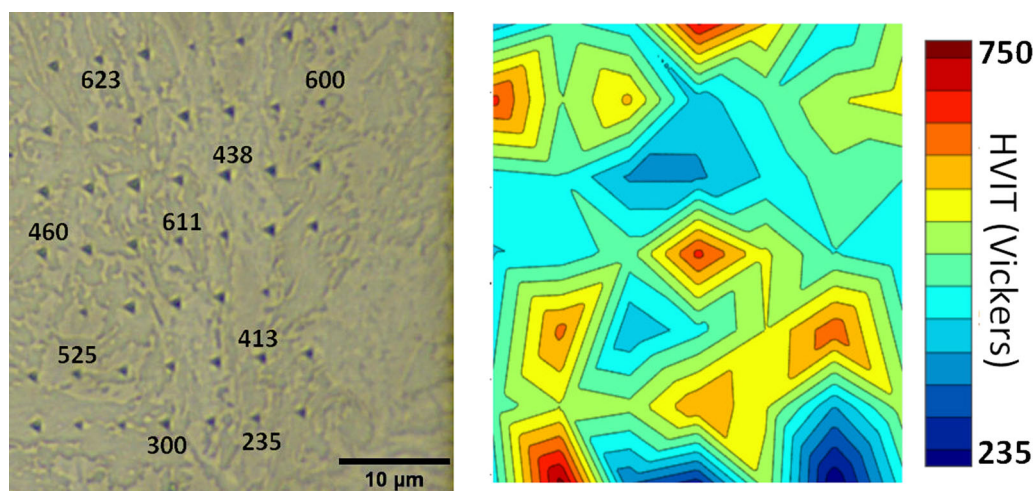

Fig. 9—Calculated hardness (HVIT) distribution map performed based on the nanoindentation.

transformation.[53] To determine the carbon concentration in austenite ($C\gamma$), the calculations of the temperature T_0' and $x_{T0'}$ (carbon concentration at T_0' temperature) were performed close to the M_s temperature. It was assumed that the concentration of carbon just before the martensite transformation is important for the evaluation of austenite stability versus temperature. The microstructure analysis confirmed that most of the austenite undergoes bainite transformation during continuous cooling. Thus, the final retained austenite content was determined by the carbon concentration in austenite at the temperature corresponding to the end of the bainite transformation (close to M_s temperature). Temperature M_s was determined using the Bayesian neural network model and the following equation[54]:

$$M_s(°C) = (764.2 - 302.6w_C - 30.6w_{Mn} - 16.6w_{Ni} - 8.9w_{Cr}$$
$$+ 2.4w_{Mo} - 11.3w_{Cu} + 8.58w_{Co} + 7.4w_W - 14.5w_{Si}) - 273.15, \quad [7]$$

where w indicates the wt pct of given chemical elements. The content of retained austenite (stable in the room temperature), taking into account the T_0' approach, was determined from the Koistinen–Marburger relationship[55]:

$$V_{\gamma r} = \exp\{-0.011(M_s^r - Tq)\}, \quad [8]$$

where $V_{\gamma r}$ is the content of retained austenite after cooling to room temperature, Tq is the lowest temperature during cooling (here 25 °C), M_s^r is the calculated M_s temperature of retained austenite based on determined ($C\gamma$) by T_0' corresponding to the temperature slightly above M_s of tested steel and Eq. [7]. To estimate the martensite fraction, the modification of Eq. [8] was applied:

$$V_{\alpha'} = \exp\{-0.011(M_s^{r(XRD)} - 25)\} - V_{\gamma(XRD)}, \quad [9]$$

where $V_{\alpha'}$ is the martensite fraction, $M_s^{r(XRD)}$ is the martensite start temperature based on ($C\gamma$) measured based on XRD data and Eq. [7], and $V_{\gamma(XRD)}$ is the austenite content measured based on XRD data. The results of the calculations are presented in Table III. To compare the obtained results of martensite fraction, the graphical image editing (GIE) was performed based on microstructure observations (image quality maps, EBSD—Figure 10 a, d) presented in further sections.

M_s—martensite start temperature; T0'—T0 temperature considering stored energy of the bainitic ferrite (400 Jmol^{-1}); $x_{T0'}$—carbon content at given T0' temperature; M_s^r—martensite start temperature of retained austenite based on $x_{T0'}$; $V_{\gamma r}$—volume fraction of retained austenite; $V_{\alpha b}$—volume fraction of bainitic ferrite; a_γ—lattice parameter of austenite; C_γ—austenite carbon

concentration; $M_s^{r(XRD)}$—martensite start temperature of retained austenite based on XRD analysis of carbon concentrations; $V_{\alpha'}$ Eq. [5]—M/A fraction based on calculations using Eq. [5]; $V_{\alpha'\ IA}$—M/A fraction based on quantitative image analysis.

Analyzing the obtained results, it was found that the T_0' ($x_{T0'}$) approach is generally comparable to the XRD results ($C\gamma = 0.68$ and $C\gamma = 0.79$, respectively, Table 4). Thus, for bainitic steels after continuous cooling, it is possible to determine $C\gamma$ in simplification assuming T_0' slightly above the calculated M_s temperature. On the other hand, M_s^r (213 °C) and $M_s^{r(XRD)}$ (180 °C) indicated that the obtained results are not exactly equal, but a difference of 30 °C may be acceptable. Both methods of determining the M/A constituents fraction are comparable and Eq. [6] can be used in the calculation of phases contents also after continuous cooling. It should be also mentioned that austenite content calculated from T_0' and Eq. [5] compared to XRD quantitative results they are practically the same (0.126 and 0.1275, respectively). To limit the empirical calculations, the austenite and martensite content was determined based on Eq. [6] and XRD data. The obtained calculations give evidence of the insufficient stability of austenite, which undergoes partial transformation to martensite after cooling to room temperature. Graphical analysis of EBSD images was performed to quantify M/A islands. Due to the presence of a martensite substructure in the coarse regions of the retained austenite, a lower value of CI, KAM, and IQ parameters was obtained. Based on the analysis of EBSD maps, the areas of occurrence of M/A islands were manually defined and outlined using GIMP and ImageJ software. According to the calculations and image analysis, the martensite content is in the range of 5.5 to 7.2 pct. Moreover, the ratio of austenite retained to martensite was found to be approx. 2.0, which indicates the significant dominance of retained austenite over martensite.

The presence of various structure constituents was also confirmed by nanoindentation measurements (Figure 9). The hardness distribution proves the high degree of differentiation of the hardness. The matrix bainitic ferrite was characterized by the lowest hardness (below the global hardness of material). The highest hardness range was identified in the areas of M/A coconstituents where the values exceeded even 600 HV. Increased hardness was also found at the boundaries of the bainitic ferrite laths. It should be mentioned that this is a calculated hardness performed under low load values and cannot be directly compared to conventional hardness measurements. Nevertheless, these results indicate that there are significant differences in the hardness of the phases, which may play a crucial role in the fracture process.

In summary, the microstructure mainly consists of bainitic ferrite laths with thicknesses in the range of 150–450 nm. There is also retained austenite with both blocky and filmy morphology with a total content of approx. 12.75 pct. As a result of the continuous cooling, part of the austenite was transformed into martensite, and the M/A constituents content in the final structure is approx. 5.5 to 7.2 pct. The addition of silicon in the tested steel effectively reduced the precipitation of
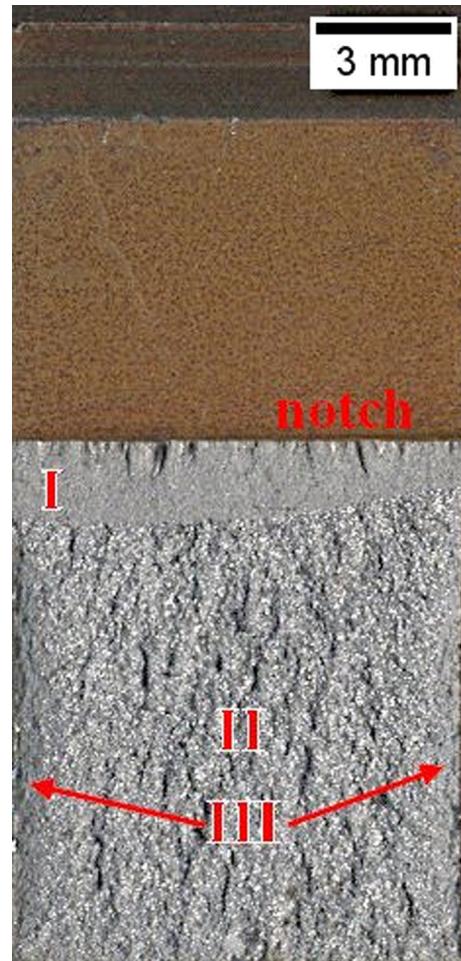

Fig. 10—Macroscopic view of the fracture topography with indicated areas (I, II, and III) of microscopic investigations.

carbides from austenite. However, carbide precipitations inside the bainitic ferrite lath were locally identified. Nevertheless, their fraction can be considered negligible.

C. Nature of Cracking and Crack Paths Analysis

The observations of topography features of fracture toughness surfaces were performed using SEM and topographic mode (secondary electrons detector) methods. Figures 5, 6 present the results of the fractographic analysis of the tested bainitic steel after fracture toughness investigations considering the various fracture zones indicated in Figure 10. Three significantly different zones are identified, labeled I, II, and III. Region I was located near the notch and covered approximately 14 pct of the entire fracture area (pre-cracked area). In turn, region II was identified in the core of the samples and region III at the edges of the samples (approximately 6–10 mm wide).

Region I (pre-cracked area) of the tested fracture topography corresponds to the initiation of main crack propagation, which is characterized by a significantly different appearance in comparison to the fracture surface (Figure 11). Overall, the dominant nature of the cracking was assessed as transcrystalline (Figure 11a).
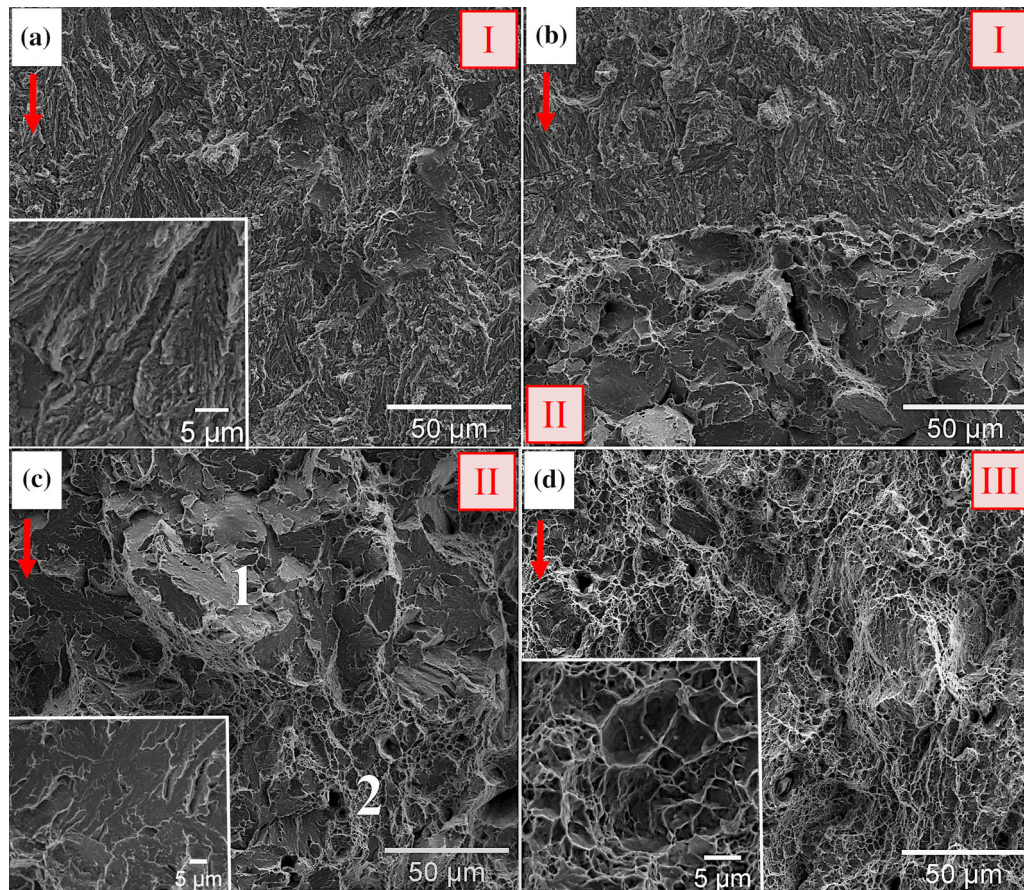
Fig. 11—Fractographic analysis of the fracture surface in the regions indicated in Fig. 10. (*a*) Region I. Dominant transcrystalline and quasi-cleavage fracture. (*b*) The boundary of regions I and II. A visible change in the nature of the fracture mechanism from quasi-cleavage to cleavage–ductile. (*c*) Region II. Visible dominant cleavage fracture and a significant part of ductile fracture. (*d*) Region III. Ductile fracture with various dimples diameters. The expanding crack fracture direction is marked with an arrow.

Table IV. Qualitative and Quantitative Analysis of the Microstructure of Tested Steel After Continuous Cooling

Calculated							XRD Data			Martensite fraction	
M_s (°C)	T_0' (°C)	$x_{T0'}$ (Wt Pct)	M_s^r (°C)	$V_{\gamma r}$	$V_{\gamma r}$	$V_{\alpha b}$	a_γ (Å)	C_γ (Wt Pct)	$M_s^{r(XRD)}$ (°C)	$V_{\alpha'}$ Equation (5)	$V_{\alpha'}$ IA
330	335	0.68	213	0.126	0.1275	0.8725	3.606	0.79	180	0.055	0.072

Apart from that, areas indicative of a partially intergranular fracture mechanism were also identified. However, it should be mentioned that this mechanism was identified only locally and represented a significantly lower fraction compared to transcrystalline fracture.

The majority of the fracture surface was characterized by a cleavage–ductile fracture, designated as region II (Figures 10 and 11bc). Also, the boundary of regions I and II is identified (Figure 11b), which indicates a sudden change in the fracture mechanisms. In area II, cleavage facets are well defined and coarser compared to the previous ones. The transcrystalline cracking process was dominant in this region. It is well known that the cleavage fracture process consists of two stages: initiation of microcrack and its propagation. It was found that brittle–cleavage fracture is observed when microcracks formed in the bainitic ferrite packets exceed the critical size and then propagate into adjacent packets.[56] Considering the dimensions of the facets and the grain size of the prior austenite (approx. 47 μm), it was stated that facets rather represent bainitic ferrite packets than the cross section of the grains (Figure 10c). Thus, the fracture topography supports the hypothesis of brittle fracture by bainitic ferrite packets and indicates their importance in the context of the fracture process. In addition to the typical cleavage fracture, areas of ductile fracture were also identified (Figure 11b, indicated as "2"). However, it should be emphasized that the ductile fracture was limited in region II. On the other hand, it constitutes a significant area fraction that should not be
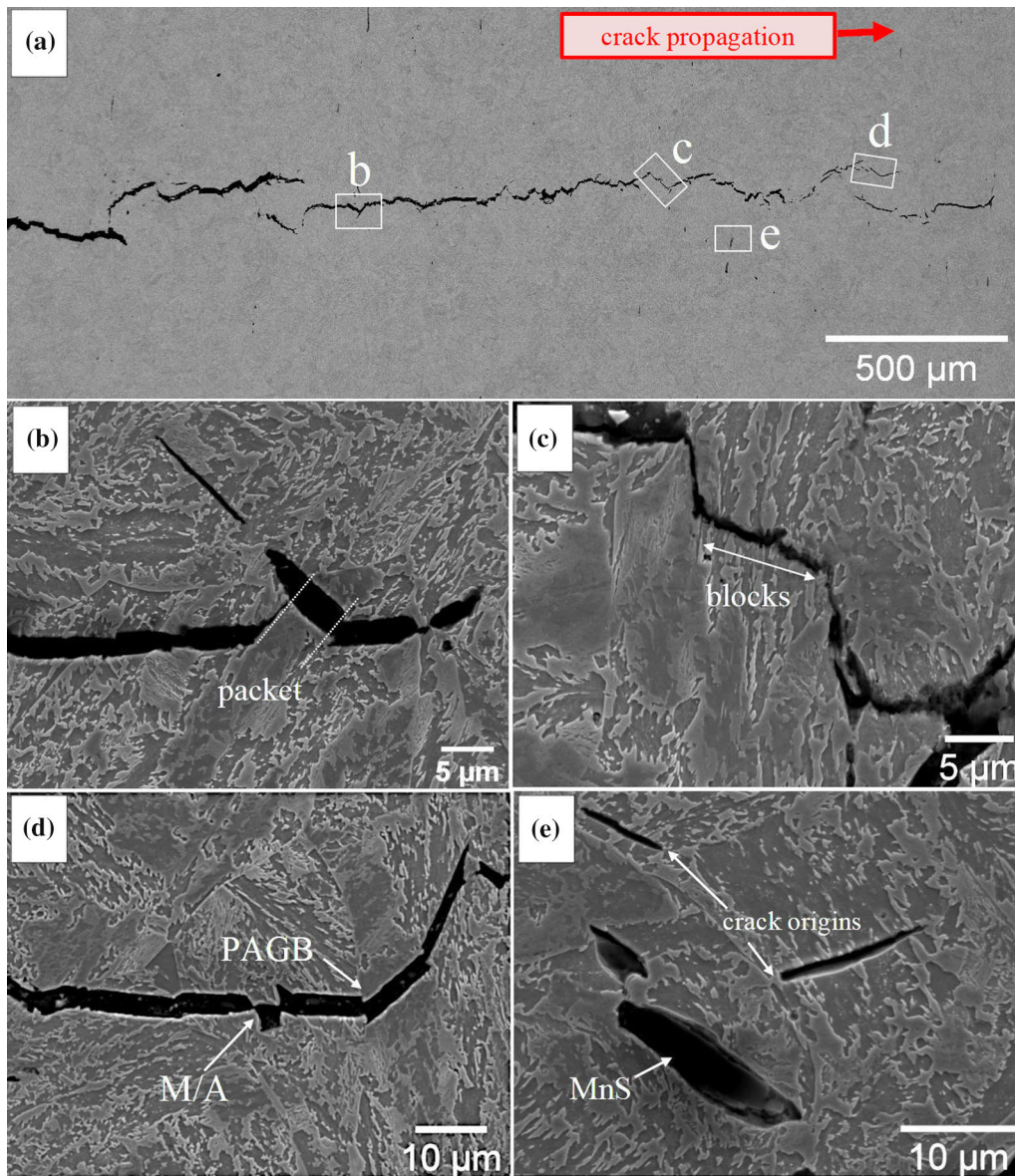
Fig. 12—(a) Macroscopic view of the crack path. (b) The change of the crack path is due to the different orientations of the bainitic ferrite packets. (c) Crack propagation through bainitic ferrite laths with the same orientation. (d) The local change in crack propagation related to the presence of M/A constituents and prior austenite grain boundary (PAGB). (e) Secondary microcracks propagating by bainitic ferrite laths with the same orientation.

neglected. The mixed nature of the fracture indicates the relatively high ductility of the tested material. The observed voids were characterized by relatively fine dimensions. Wang et al.[57] stated that the interphase between fine-grained bainitic ferrite and M–A constituent is prone to microvoid initiation, which is explained by the slight difference in hardness and preventing their coalescence by the matrix. In terms of the current investigations, the area fraction of the ductile fracture is generally higher compared to the fraction of the M/A constituent indicated in Table IV ($V_{\alpha'} = 5.5 \div 7.2$ pct). This result points to other microstructural features influencing the formation of microvoids and ductile fracture mode. Moreover, in the

area near the edge of the samples (region III—Figure 11d), a ductile fracture mode was identified. Similarly, the ductile fracture mechanism was also observed in other investigations on low-carbon bainitic rails intended for rails applications.[5] It has also been found that the diameters of the microvoids are varied (in the range of 0.2 to 10 μm), and a minority of them contain precipitations and inclusions.

To determine the influence of the microstructure morphology on the crack path, observations on the cross section after the fracture arrest were performed. It was found that in addition to the main crack, secondary cracks also propagated (Figure 12a). For this reason, it is difficult to unequivocally define the top of the main crack.

It was stated that the shape of the crack tip during the blunting stage is dependent on the strain hardening properties of materials and the yield–tensile ratio.[58] Tested material is characterized by a relatively low yield–tensile ratio (0.56–0.68, Table II), thus, it should be susceptible to crack tip blunting in the wide area behind the crack tip. However, as can be seen in Figure 11a, this mechanism does not occur in the case of identified crack tips. The analysis of changes in the crack path in relation to the microstructure was performed [Figures 12(b) through (e)]. Global changes in the direction of crack propagation in the area of the orientation changes of the bainitic ferrite packet were identified. Then, the crack spread through the present packet and again changed direction after crossing the packet boundary. It was also observed that the blocks of bainitic ferrite laths did not significantly affect the crack path (Figure 12c). On the other hand, packet boundaries and other structural constituents influenced local changes in crack propagation (Figure 12d), which is consistent with the other results.[19] A change in the crack path after reaching the grain boundary of the prior austenite was also noticed. In addition, the crack path propagation temporarily changed after exceeding the M/A constituent. Secondary cracks were identified in the vicinity of the main fracture (Figure 12e). Secondary cracks propagate through laths in bainitic ferrite blocks. Their probable origins were voids or microcracks at the packet boundary (especially in M/A areas), and their development led to propagation in the most favorable direction avoiding the energy barrier, i.e., through low- and middle-angle boundaries (blocks). Moreover, the visible non-metallic inclusions (manganese sulfides) did not affect the propagation of secondary cracks. Thus, it was found that probably the cracking process is more influenced by the microstructure morphology than the presence of inter-metallic and non-metallic inclusions.

The crack path was also analyzed concerning the orientation of the crystallographic units (Figure 13). To reveal the grain boundaries of the prior austenite, the misorientation angles in the range of 20 to 40 deg were emphasized and the grain boundary reconstruction was performed[59]—Figures 13b and Figure 13(c), respectively. The grain indicated a "3" contained a complex crack path which was associated with the different orientations of the bainitic ferrite blocks. After reaching grains "3" and "2," the crack propagated through the bainitic packet without visible changes in the direction of cracking. Then, after crossing grain "1," the crack partially propagated along the grain boundary of the prior austenite. Moreover, misorientation angles along the crack were measured to identify energy barriers affecting crack propagation (Figure 14). The approximate range of blocks boundaries (~ 20 deg—blue line) and packet boundaries (above 45 deg—red line) was
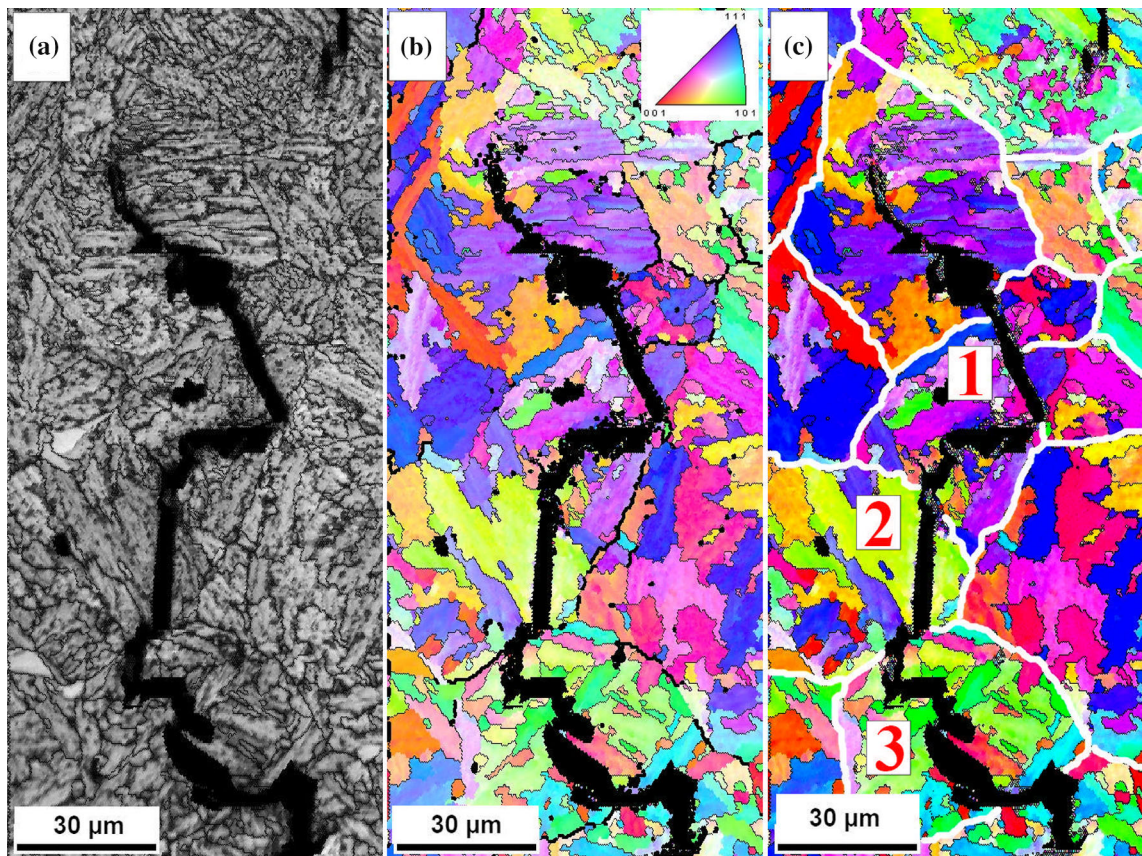

Fig. 13—Crack path view. (*a*) Image quality map. (*b*) Inverse pole figure map. (*c*) Inverse pole figure map with reconstructed prior austenite grain boundaries. Analysis area 82 μm × 187 μm, step size 0.47 μm.
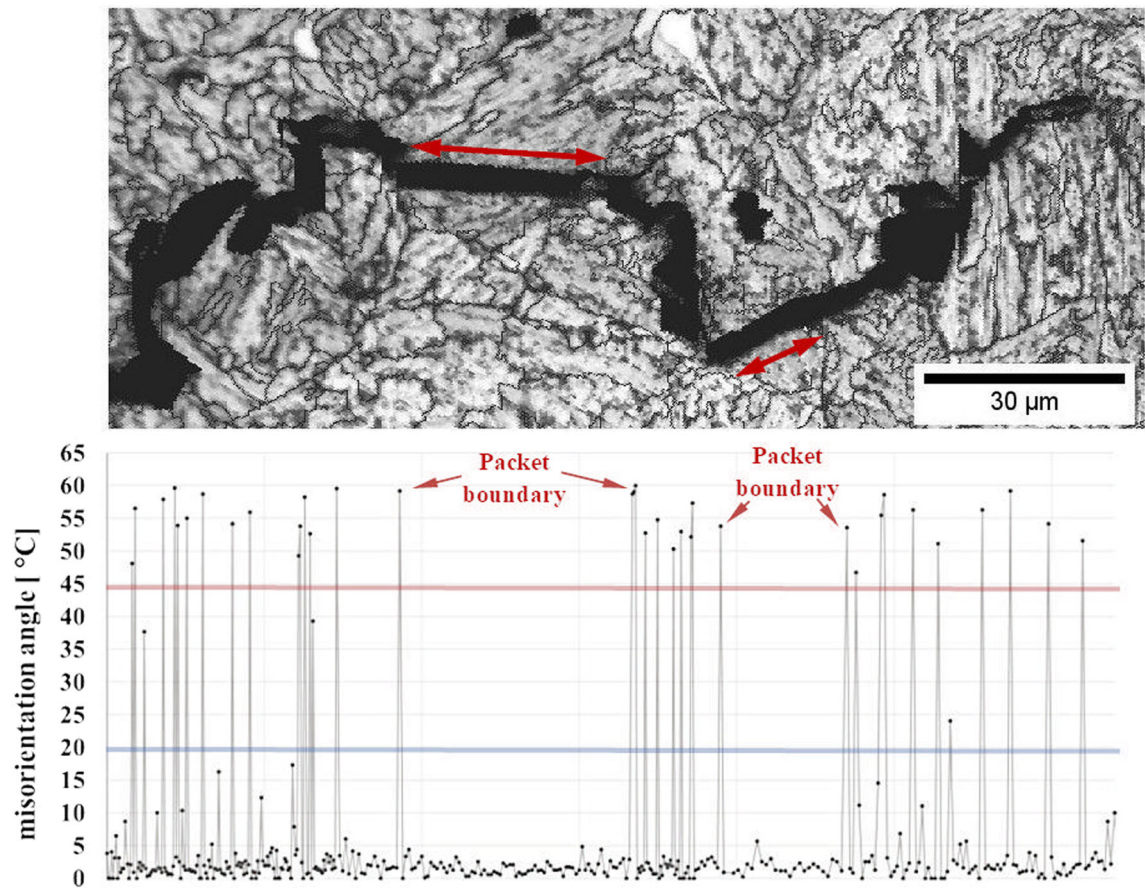
Fig. 14—The crack path concerning the measured misorientation angles. Middle-angle values are marked with a blue line and high-angle values with a red line. Analysis area 82 × 187 μm, step size 0.47 μm (Color figure online).
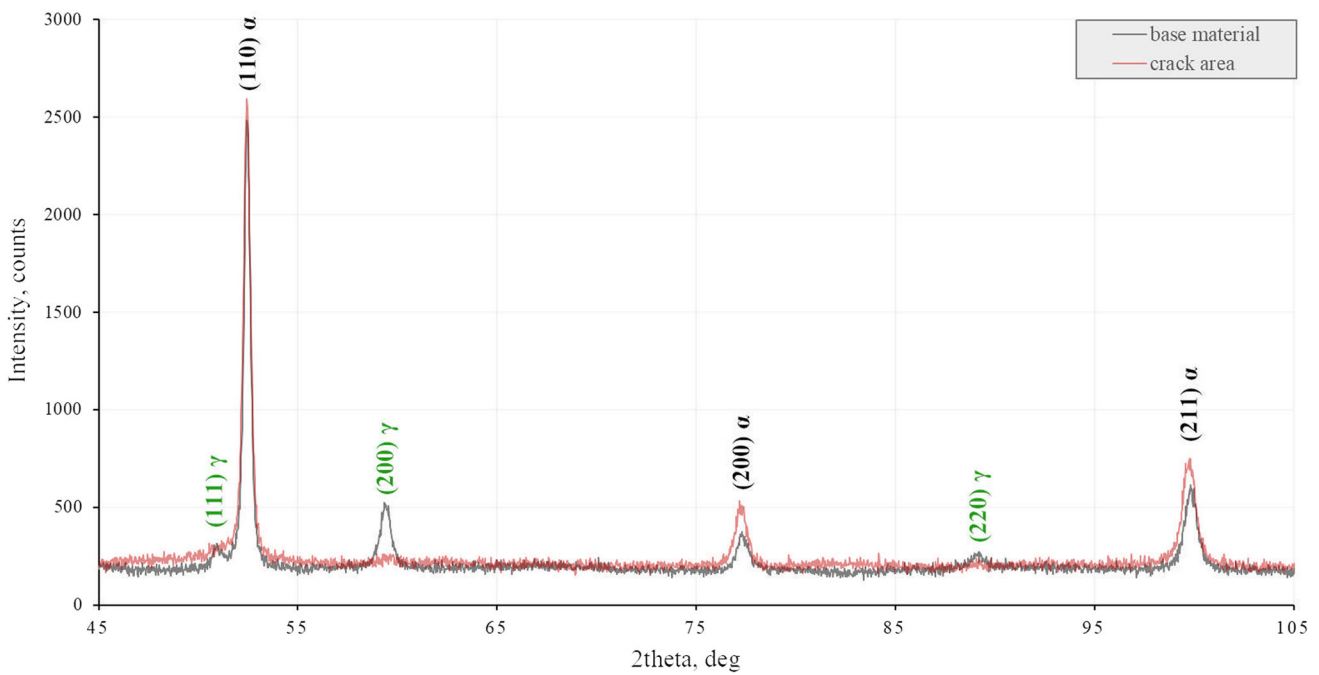

Fig. 15—Comparison of the XRD profiles of the base material (gray) and the area at the assumed crack tip (red) (Color figure online).
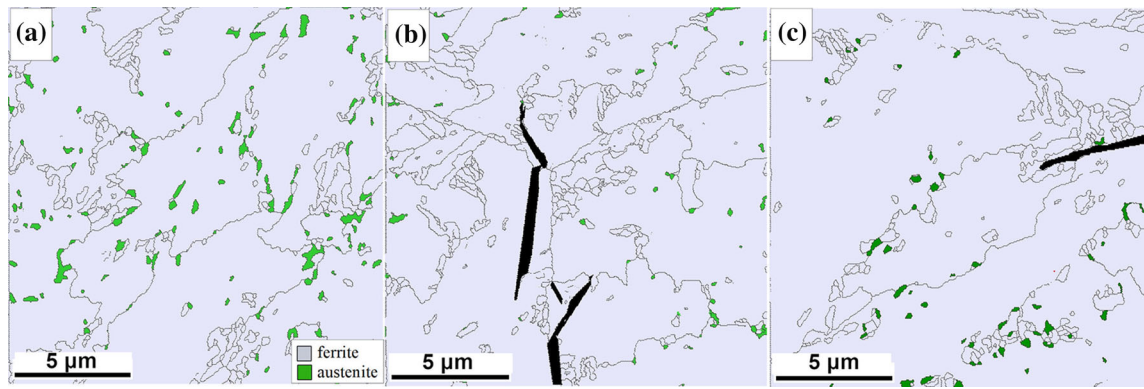
Fig. 16—Phase distribution maps of ferrite (BCC—gray) and austenite (FCC—green) were obtained by the EBSD method. (*a*) Base material. (*b*), (*c*) Crack tips in different tested areas. Analysis area 16 μm × 16 μm, step size 40 nm (Color figure online).

indicated. The measured fracture path did not exhibit a high proportion of the boundaries between the blocks, which results from the parameters of the EBSD analysis (magnification and step size). In the case of high-angle boundaries, including packet boundaries, there is a correlation between the cracking path. It should be noted that the changes in the crack path occurred after encountering the high-angle boundary, usually corresponding to the packet boundaries. Two bainitic ferrite packets with boundaries of ~ 59 and ~ 53 deg were identified, respectively. No significant changes in crack propagation occurred in the low-angle misorientation regions. However, it should be emphasized that misorientation angles were measured near the crack, thus they should be considered rather as an estimation. Nevertheless, these results confirm the close relationship between misorientation angles and crack propagation.

D. *The Microstructure Evolution Prior the Crack Tip*

It is well-known that crack tip causes stresses and strain fields, which values are dependent on the material properties.[60,61] Therefore, it is plausible that there is a probability that the strain and stress field caused by the crack tip may affect the microstructure evolution and thus have a significant impact on the fracture process. It was found that during fracture, the transformation from retained austenite to martensite may occur[24] at the crack tip. Especially, in terms of TRIP-assisted multi-phase steels, a complete austenite transformation into martensite that occurs in the fracture process zone (FPZ) was observed.[62] It should be mentioned that the rate of the martensitic transformation during the fracture process depends on the retained austenite stability.[63] In the current research, the average carbon content in retained austenite is approx. 0.79 pct, which indicates its potentially high stability. However, it should be noticed that the carbon content of the austenite is characterized by a heterogeneous distribution.[64] To qualitatively assess the occurrence of martensitic transformation of retained austenite near the crack tip, an XRD micro-diffraction was performed. Based on the obtained XRD profile, it was found that in

the crack tip area there are no clearly visible peaks of austenite, unlike in the base material (Figure 15). This proves that the stresses and strain field induced by the crack tip were practically sufficient to complete martensitic transformation. Another evidence was the microstructure observations on the cross section of the sample using the EBSD method (Figure 16). It was found that the retained austenite was not maintained in the region of about 4–5 μm from the crack tip [Figures 16(b), (c)]. This area may also be classified with the FPZ. On the other hand, it should also be mentioned that the EBSD technique used did not reveal the presence of austenite with film-like morphology due to its nanoscale dimensions, which is characterized by higher stability and carbon concertation compared to blocky morphology.[65] On the other hand, the XRD profile did not reveal any significant content of austenite in the fracture area, thus it may be concluded that it underwent a martensitic transformation.

To evaluate the influence of crack propagation on bainitic ferrite morphology at the crack tip the EBSD analysis was conducted and compared to the base material (Figure 17). The image quality maps confirmed the presence of the M/A constituents [Figures 17(a), (d)]. The microstructure of the base material consists of blocks of bainitic ferrite of the same orientation and refined areas of various orientations that can be classified as M/A constituents, retained austenite, or ferrite sub-grains [Figure 17(b)]. Moreover, the Grain Misorientation Map indicated that refined areas are characterized by a significantly higher degree of misorientation [Figure 17(c)]. The crack tip observations clearly indicate the evolution of the bainitic ferrite structure. A significantly higher proportion of M/A constituents and/or ferrite sub-grains were identified directly in the crack tip area [Figures 17(e), (f)]. The probability of sub-grain and cell structures formation was also proposed in investigations.[12] On the other hand, the presence of blocky retained austenite was excluded in the fracture process zone [Figure 17(c)].

In terms of a typical value for instrumental diffraction peak broadening in a conventional X-ray diffractometer, only crystallite with a size lower than 100 nm can be
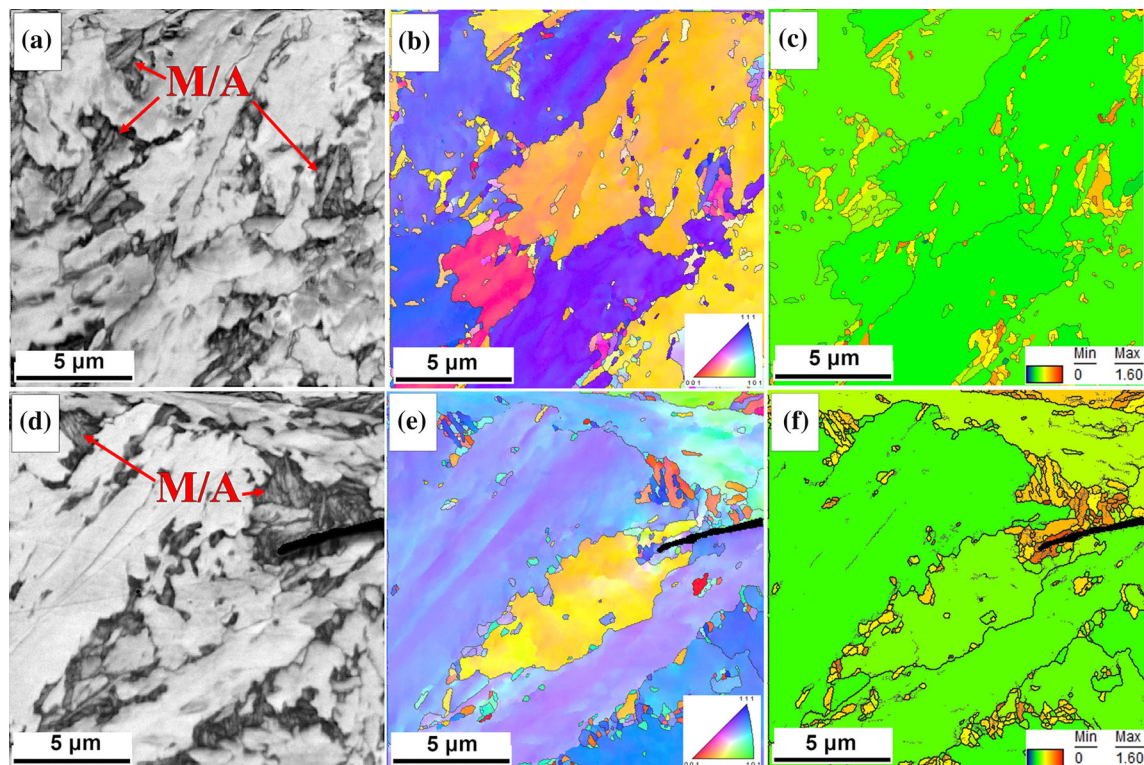
Fig. 17—A comparative EBSD analysis. (*a*), (*d*) Image quality maps of base material and crack tip area, respectively. (*b*), (*e*) Inverse pole figure map of base material and crack tip area, respectively. (*c*), (*f*) Grain Misorientation Maps of base material and crack tip area, respectively. Analysis area 16 μm $\times$ 16 μm, step size 40 nm.

Table V.   Calculation Results of the Crystallite Size and Dislocation Density Based on the XRD Profiles are Shown in Fig. 17

Tested Area	Crystallite Size [nm]	Strain ε [Pct]	The Magnitude of Burgers Vector	k constant	Dislocation Density ρ [m^{-2}]
Base Material	87	0.22	1.432	14.4	3×10^{-17}
Crack tip	42	0.17	1.433	14.4	2×10^{-17}

effectively measured. Moreover, crystallite size determined by XRD and laths thickness of bainitic ferrite is not equal.[66] Because a conventional diffractometer was used, the size of the crystallites only indicates the possibility of refining the bainitic ferrite laths and forming sub-grains due to the deformation caused by the crack tip (Table V). This hypothesis is supported by microstructural investigations using EBSD [Figs. 16(e) and (f)]. It was determined that in the crack area the dislocation density of bainitic ferrite decreased compared to the base material (Table V). A similar result was also found in the research on cyclic deformation,[12] therefore also in the case of the area crack tip/matrix interaction, the change in dislocation density may be caused by the formation of sub-grains. Also, it is another observation supporting this hypothesis along with the size of the crystallites. On the other hand, the result of the dislocation density determination should be considered carefully and rather as an estimation due to the not perfect fit of linear functions in W–H plots (Figure 18).

E. *Discussion—The Crack Path Evolution and Influence of Crack Tip*

It was proven that the continuously cooled low-carbon bainitic rail achieves a significantly higher toughness compared to conventional pearlitic rail steel grades (Table III). Moreover, the tested continuously cooled rail is characterized by a comparable level of fracture toughness compared to another bainitic rail grade (J6).[4,48] These results are caused both by the different mechanical properties of these rail materials (indicated in[16]) and various microstructures. Low-carbon bainitic steels are characterized by several different morphologies,[21] where the refinement degree of the structural components is also crucial. In the current study, low-carbon bainitic steel with the sub-micrometric dimensions of bainitic ferrite laths (150–450 nm) was evaluated, along with retained austenite with filmy and blocky morphology (12.75 pct in total), as well as low content of M/A constituents (5.5 to 7.2 pct). The influence of the microstructure on the cracking mechanisms was indicated and the evolution of the
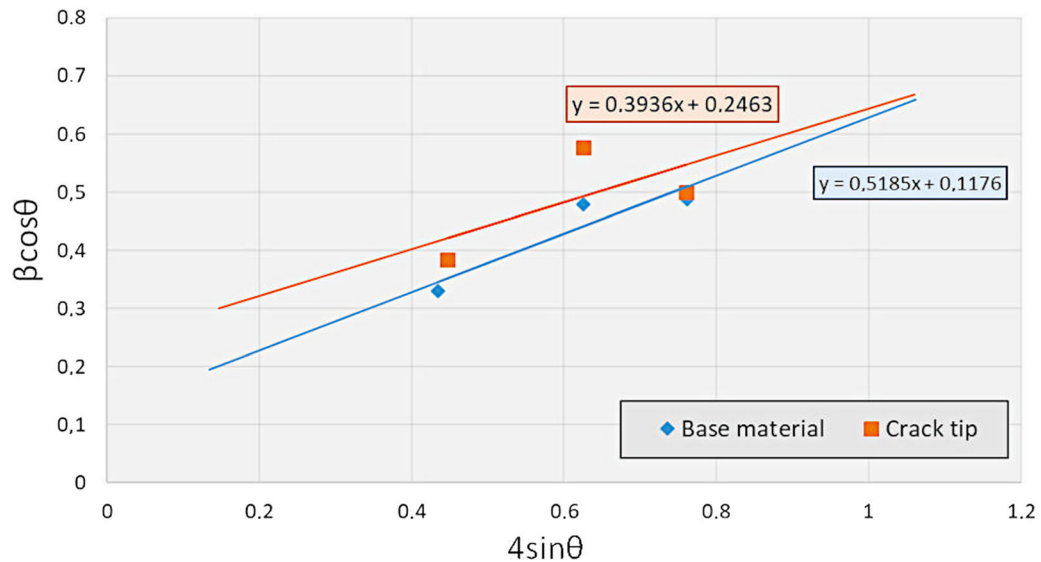
Fig. 18—Williamson–Hall plots of base material and crack area considering bainitic ferrite.

microstructure in the area of the crack tip was determined (Figure 19). A different mode of cracking was found in the near-notch zone, where a quasi-cleavage fracture occurred.[67,68] In this area, the notch effect was of significant importance, which was confirmed by the number of secondary cracks and longitudinal ridges. The facets were characterized by lath-like ridges and step lines, which were related to the boundaries of the crystallographic units. Due to the influence of the notch, this area was less sensitive to the morphology of the structure, and the fracture process directly related to microstructure dominated on the fracture surface (region II, Figure 8). The identified cleavage–ductile fracture resulted from the microstructural features and the propagation of microcracks formed in the bainite packets and M/A constituents. In general, the dimensions of the specific cleavage facets correspond to the dimensions of the bainite packets. It was noticed that the global crack path change occurs at packet boundaries and prior austenite grains, which is also supported by other work.[19] It follows that the dimensions of the bainitic packets play a significant role in the fracture process. It is worth mentioning that bainite packets are characterized by HABs and constitute an energy barrier for fracture processes. Additionally, in work[33] was stated that the density of HABs (above 45 deg) effectively improves the toughness. Thus, this again proves the importance of reducing the packet dimensions, which leads to an increase in the HABs density. Also, it seems obvious that the refinement of the prior austenite grain boundaries enhances the fracture toughness of bainitic steels. It was hypothesized that the mode of cracking of bainitic steels (cleavage or ductile) depends on the angles of misorientation between the blocks and the specific crystallographic variants. Considering that the fracture process is associated with the desire to minimize energy, the low-angle boundaries should lead to easier transcrystalline cleavage fracture. In contrast, higher angles between the blocks will allow

for coagulation and microvoids development which will contribute to the ductile fracture mode. During the cracking process, the features influencing the local changes in the direction of crack propagation were also indicated. Although their influence is not as pronounced as that of packet boundaries and PAGB, they also significantly contribute to the fracture process. The fracture process involves nucleation and microcrack propagation. Privileged sites for microcracks and microvoids nucleation are the M/A constituents.[13,23,24] It should also be mentioned that it is possible to reduce hard martensitic phases or M/A constituents by modifying the chemical composition, for example, by adding boron.[69] The microcracks are also formed at the packet boundaries and their development led to propagation in the most favorable direction avoiding the energy barrier (through blocks). Moreover, it should be emphasized that in the fracture process zone caused by the crack tip, a significant evolution of the microstructure occurs. In the present research, it was clearly determined that in this zone a practically complete transformation of retained austenite undergoes. However, it cannot be ruled out that there is a certain content of filmy austenite in the FPZ. Therefore, the evaluation of the evolution of filmy retained austenite in the FPZ requires further research. There is no doubt about the complete transformation of the blocky retained austenite at a distance of about 4 to 5 μm from the crack tip. In turn, the transformed austenite into martensite accumulated the damage and caused the development of a void nucleation mechanism.[62] Moreover, the transformation of high carbon-retained austenite led to high strength and brittle martensite which contributes to easier cracking.[63] In the cracking process, the strain caused by the crack tip is also of particular importance. The influence of FPZ has explained above, while evolution in the microstructure also undergoes in the area adjacent to the crack tip. It was found that the dislocation density
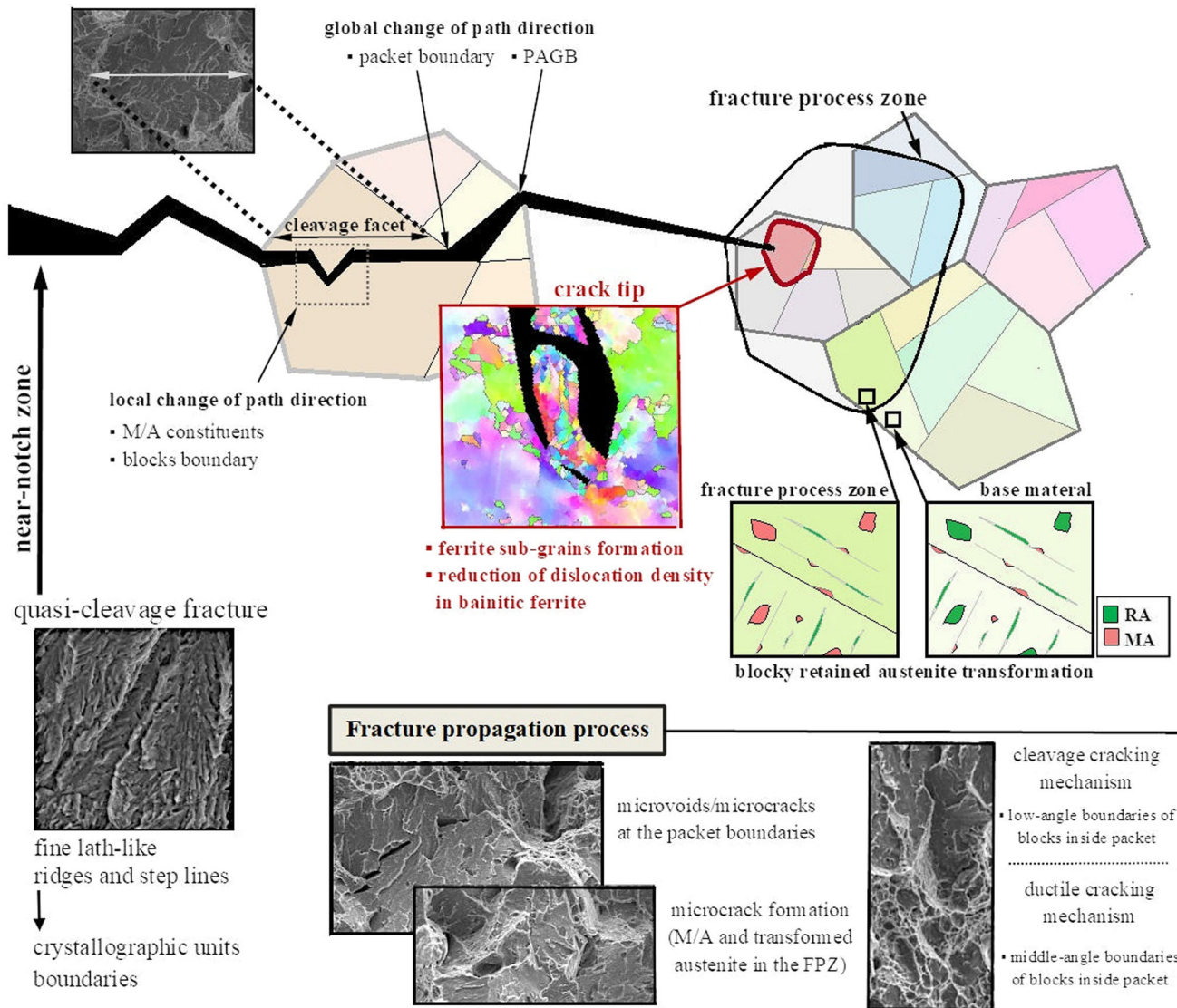
Fig. 19—The hypothesis of the fracture propagation process and microstructure evolution in the fracture process zone of low-carbon bainitic steel after the continuous cooling process.

decreased at the crack tip, which was supported by the formation of sub-grains.[12]

Due to the technological properties and the prospects for industrialization,[70] bainitic steels subjected to continuous cooling are vastly promising. The variety of bainite morphology and different proportions of phases after continuous cooling directly influence the mechanisms of their fracture. This study confirmed that there are critical structural features that determine the fracture toughness and nature of cracking. Thus, optimization of the structure morphology is a prerequisite for a significant improvement in fracture toughness, while maintaining the possibility of natural cooling after the manufacturing process. However, it should be emphasized that the process of continuous cooling also determines the differentiation of the morphology of the structure in the rail cross section (head, web, and foot). In these studies, the core of the rail head was analyzed, where the structure slightly differed from the running surface. Future research should also focus on the analysis of structural changes as a function of distance from the running surface. The residual stresses associated with the phase transformation may also play a crucial role, which may also tend to be unevenly distributed over the rail cross section.

IV. CONCLUSIONS

Based on the performed research, the following conclusions and perspectives for the improvement of fracture toughness were formulated:

- Investigated low-carbon bainitic steel after continuous cooling is characterized by a higher fracture toughness (K_Q = 58.9 MPa√m) in comparison to a conventional pearlitic grade of steels intended for rails production. The K_Q value was also comparable to the other grade of bainitic rail steel (J6). The results indicate that, in terms of fracture toughness, the designed bainitic rail after natural continuous cooling may be considered as an significant competitor to pearlitic steel grades.
- Initial microstructure of the bainitic steel contained sub-micrometric bainitic ferrite laths (150 to 450 nm), blocky and filmy retained austenite, and a low fraction of M/A.
- In the near-notch area, a quasi-cleavage fracture mode was found. In contrast, majority of the fracture surfaces (region II) exhibited a transcrystalline cleavage–ductile fracture mode. A ductile fracture was identified at the edges of the tested samples.
- The change in the direction of the crack propagation path was related to the boundaries of the bainite packets and the boundaries of the prior austenite grains. Local, minor changes in the direction of propagation also occurred after exceeding M/A constituents and block boundaries. A moderate number of non-metallic inclusions did not play a significant role in the fracture process.
- In the Fracture Process Zone (approx. 4 to 5 μm from the crack tip), the retained blocky austenite was transformed into martensite. In the close-tip area, a decrease in dislocation density in bainitic ferrite and the formation of ferrite sub-grains was found.
- The perspective of improving fracture toughness of investigated bainitic steel should focus on controlling the grain size of the prior austenite and reducing the size of the bainite packets. The origin of the microcracks were the M/A regions and the areas of transformed blocky retained austenite (into brittle martensite) in the Fracture Process Zone. Therefore, it is also particularly important to control the stability of the retained austenite and its morphology and dimensions.

ACKNOWLEDGMENTS

CONFLICT OF INTEREST

On behalf of all authors, the corresponding author states that there is no conflict of interest.

OPEN ACCESS

DATA AVAILABILITY

The datasets generated during and/or analysed during the current study are available from the corresponding author on reasonable request.

REFERENCES

1. A. Kumar, S.K. Makineni, A. Dutta, C. Goulas, M. Steenbergen, R.H. Petrov, and J. Sietsma: *Mater. Sci. Eng. A*, 2019, vol. 759, pp. 210–13.
2. M.N. Georgiev and T.V. Simeonova: *Met. Sci. Heat Treat.*, 2018, vol. 60, pp. 464–70.
3. O. Hajizad, A. Kumar, Z. Li, R.H. Petrov, J. Sietsma, and R. Dollevoet: *Metals (Basel)*, 2019, vol. 9, p. 778.
4. K. Sawley and J. Kristan: *Fatigue Fract. Eng. Mater. Struct.*, 2003, vol. 26, pp. 1019–29.
5. H.A. Aglan, Z.Y. Liu, M.F. Hassan, and M. Fateh: *J. Mater. Process. Technol.*, 2004, vol. 151, pp. 268–74.
6. H. Aglan, M. Hassan, Z. Liu, M. Bhuyan, and M. Fateh: *J. Mater. Sci.*, 2004, vol. 39, pp. 4305–07.
7. S.M. Hasan, D. Chakrabarti, and S.B. Singh: *Wear*, 2018, vol. 408–409, pp. 151–59.
8. F.H. Çakir and O.N. Çelik: *Met. Sci. Heat Treat.*, 2017, vol. 59, pp. 289–93.
9. B. Gao, Z. Tan, Y. Tian, Y. Liu, R. Wang, G. Gao, J. Wang, and M. Zhang: *Steel Res. Int.*, 2021, p. 2100494.
10. S.M. Hasan, M. Ghosh, D. Chakrabarti, and S.B. Singh: *Mater. Sci. Eng. A*, 2020, vol. 771, p. 138590.
11. B. Adamczyk-Cieślak, M. Koralnik, R. Kuziak, T. Brynk, T. Zygmunt, and J. Mizera: *Mater. Sci. Eng. A*, 2019, vol. 747, pp. 144–53.
12. B. Adamczyk-Cieślak, M. Koralnik, R. Kuziak, K. Majchrowicz, and J. Mizera: *Metall. Mater. Trans. A*, 2021, vol. 52A, pp. 5429–42.
13. O. Hajizad, A. Kumar, R.H. Petrov, J. Sietsma, R. Dollevoet, and Z. Li: *Comput. Mater. Sci.*, 2022, vol. 202, p. 110965.
14. S. Das and A. Haldar: *Metall. Mater. Trans. A*, 2014, vol. 45A, pp. 1844–54.
15. M. Shah, S.K. Das, and S.G. Chowdhury: *Metall. Mater. Trans. A*, 2019, vol. 50, pp. 2092–102.
16. A. Królicka, G. Lesiuk, K. Radwański, R. Kuziak, A. Janik, R. Mech, and T. Zygmunt: *Int. J. Fatigue*, 2021, vol. 149, p. 106280.
17. B. Adamczyk-Cieślak, M. Koralnik, R. Kuziak, K. Majchrowicz, T. Zygmunt, and J. Mizera: *J. Mater. Eng. Perform.*, 2021, https://doi.org/10.1007/s11665-021-06547-w.

18. H. Terasaki and Y. Komizo: *Metall. Mater. Trans. A*, 2013, vol. 44A, pp. 2683–89.
19. H. Terasaki, Y. Shintome, Y. Komizo, M. Ohata, K. Moriguchi, and Y. Tomio: *Metall. Mater. Trans. A*, 2015, vol. 46A, pp. 2035–39.
20. Y. Huang, A. Zhao, J. He, X. Wang, Z. Wang, and L. Qi: *Int. J. Miner. Metall. Mater.*, 2013, vol. 20, pp. 1155–63.
21. K. Radwański: *Arch. Civ. Mech. Eng.*, 2016, vol. 16, pp. 282–93.
22. T. Furuhara, H. Kawata, S. Morito, and T. Maki: *Mater. Sci. Eng. A*, 2006, vol. 431, pp. 228–36.
23. F.G. Caballero, H. Roelofs, S. Hasler, C. Capdevila, J. Chao, J. Cornide, and C. Garcia-Mateo: *Mater. Sci. Technol.*, 2012, vol. 28, pp. 95–102.
24. S.B. Zhou, F. Hu, W. Zhou, L. Cheng, C.Y. Hu, and K.M. Wu: *J. Mater. Res. Technol.*, 2021, vol. 14, pp. 1021–34.
25. X.Z. Zhang and J.F. Knott: *Acta Mater.*, 1999, vol. 47, pp. 3483–95.
26. P. Zhao, B. Zhang, C. Cheng, R.D.K. Misra, G. Gao, B. Bai, and Y. Weng: *Mater. Sci. Eng. A*, 2015, vol. 645, pp. 116–21.
27. G. Gao, H. Zhang, X. Gui, P. Luo, Z. Tan, and B. Bai: *Acta Mater.*, 2014, vol. 76, pp. 425–33.
28. P. Zhao, G. Gao, R.D.K. Misra, and B. Bai: *Mater. Sci. Eng. A*, 2015, vol. 630, pp. 1–7.
29. X. Gui, K. Wang, G. Gao, R.D.K. Misra, Z. Tan, and B. Bai: *Mater. Sci. Eng. A*, 2016, vol. 657, pp. 82–85.
30. J.P. Liu, Y.Q. Li, J. Jin, Y.H. Zhang, F.S. Liu, R. Su, B. Narayanaswamy, and Q.Y. Zhou: *Mater. Today Commun.*, 2020, vol. 25, p. 101531.
31. V.T.T. Miihkinen and D.V. Edmonds: *Mater. Sci. Technol.*, 1987, vol. 3, pp. 441–49.
32. B. Guo, L. Fan, Q. Wang, Z. Fu, Q. Wang, and F. Zhang: *Metals (Basel)*, 2016, vol. 6, p. 256.
33. B.B. Wu, X.L. Wang, Z.Q. Wang, J.X. Zhao, Y.H. Jin, C.S. Wang, C.J. Shang, and R.D.K. Misra: *Mater. Sci. Eng. A*, 2019, vol. 745, pp. 126–36.
34. B. Chhajed, K. Mishra, K. Singh, and A. Singh: *Mater. Charact.*, 2022, vol. 192, p. 112214.
35. L. Morales-Rivas, A. Azadi, and E. Kerscher: *Int. J. Fatigue*, 2023, vol. 166, p. 107219.
36. R. Kuziak: *Hybrid Technology of the Production of Standard Gauge Rails Characterised by Enhanced Durability in Service, Accounting for the Future Trends. Final Report.*, 2018.
37. F.G. Caballero, H.K.D.H. Bhadeshia, K.J.A. Mawella, D.G. Jones, and P. Brown: *Mater. Sci. Technol.*, 2001, vol. 17, pp. 512–16.
38. H.K.D.H. Bhadeshia: *Proc. R. Soc. A*, 2010, vol. 466, pp. 3–18.
39. A. Królicka, K. Radwański, R. Kuziak, T. Zygmunt, and A. Ambroziak: *J. Constr. Steel Res.*, 2020, vol. 175, p. 106372.
40. A. Królicka, A. Żak, R. Kuziak, K. Radwański, and A. Ambroziak: *Mater. Sci.*, 2021, vol. 39, pp. 615–25.
41. ASTM International, West Conshohocken, PA, 2018.
42. A. Khorsand Zak, W.H. Abd. Majid, M.E. Abrishami, and R. Yousefi: *Solid State Sci.*, 2011, vol. 13, pp. 251–56.
43. G.K. Williamson and R.E. Smallman: *Philos. Mag.*, 1956, vol. 1, pp. 34–46.
44. P. Thirathipviwat, G. Song, J. Bednarcik, U. Kühn, T. Gemming, K. Nielsch, and J. Han: *Prog. Nat. Sci. Mater. Int.*, 2020, vol. 30, pp. 545–51.
45. D.J. Dyson and B. Holmes: *J. Iron Steel Inst.*, 1970, vol. 208, pp. 469–74.
46. A. Małachowska, P. Sokołowski, G. Paczkowski, T. Lampke, and A. Sajbura: *J. Therm. Spray Technol.*, 2022, vol. 31, pp. 1330–41.
47. P.I. Christodoulou, A.T. Kermanidis, and G.N. Haidemenopoulos: *Theor. Appl. Fract. Mech.*, 2016, vol. 83, pp. 51–59.
48. H.A. Aglan: *Fatigue Crack Growth and Fracture Behavior of Bainitic Rail Steels, DOT/FRA/ORD-11/17, 2011*, Washington, 2011.
49. U.P. Singh, B. Roy, S. Jha, and S.K. Bhattacharyya: *Mater. Sci. Technol.*, 2001, vol. 17, pp. 33–38.
50. Progr. MAP_STEEL_MUCG83, https://www.phase-trans.msm.cam.ac.uk/map/steel/programs/mucg83.html.
51. H.K.D.H. Bhadeshia: *Bainite in Steels. Theory and Practice*, 3rd ed. CRC Press, Taylor & Francis Group, Boca Raton, 2015.
52. F.G. Caballero and H.K.D.H. Bhadeshia: *Curr. Opin. Solid State Mater. Sci.*, 2004, vol. 8, pp. 251–57.
53. H.K.D.H. Bhadeshia: *Mater. Sci. Eng. A*, 2004, vol. 378, pp. 34–39.
54. C. Capdevila, F.G. Caballero, and C.G. de Andrés: *ISIJ Int.*, 2002, vol. 42, pp. 894–902.
55. D.P. Koistinen and R.E. Marburger: *Acta Metall.*, 1959, vol. 7, pp. 59–60.
56. K. Shi, H. Hou, J.-B. Chen, L.-T. Kong, H.-Q. Zhang, and J.-F. Li: *Steel Res. Int.*, 2016, vol. 87, pp. 165–72.
57. Y. Wang, Q. Wang, L. Liu, and W. Xu: *Mech. Adv. Mater. Struct.*, 2015, vol. 22, pp. 591–96.
58. T. Tagawa, T. Kawabata, T. Sakimoto, Y. Kayamori, M. Ohata, Y. Yamashita, E. Tamura, H. Yoshinari, S. Aihara, F. Minami, H. Mimura, and Y. Hagihara: *Eng. Fract. Mech.*, 2014, vol. 128, pp. 157–70.
59. A. Królicka, A. Janik, A. Żak, and K. Radwański: *Mater. Sci.*, 2021, vol. 39, pp. 188–99.
60. J.R. Rice and G.F. Rosengren: *J. Mech. Phys. Solids*, 1968, vol. 16, pp. 1–2.
61. C.F. Shih: *J. Mech. Phys. Solids*, 1981, vol. 29, pp. 305–26.
62. G. Lacroix, T. Pardoen, and P.J. Jacques: *Acta Mater.*, 2008, vol. 56, pp. 3900–13.
63. P. Jacques: *Acta Mater.*, 2001, vol. 49, pp. 139–52.
64. C. Garcia-Mateo, F.G. Caballero, M.K. Miller, and J.A. Jimenez: *J. Mater. Sci.*, 2012, vol. 47, pp. 1004–10.
65. A. Królicka, A.M. Żak, and F.G. Caballero: *Mater. Des.*, 2021, vol. 211, p. 110143.
66. C. Garcia-Mateo, J.A. Jimenez, B. Lopez-Ezquerra, R. Rementeria, L. Morales-Rivas, M. Kuntz, and F.G. Caballero: *Mater. Charact.*, 2016, vol. 122, pp. 83–89.
67. J. Fellows: *Metals Handbook, Fractography and Atlas of Fractorgrphs*, 8th ed. American Society for Metals, Ohio, 1974.
68. L. Cho, P.E. Bradley, D.S. Lauria, M.L. Martin, M.J. Connolly, J.T. Benzing, E.J. Seo, K.O. Findley, J.G. Speer, and A.J. Slifka: *Acta Mater.*, 2021, vol. 206, p. 116635.
69. K.F. Rodríguez-Galeano, R. Rodríguez-Baracaldo, A. Mestra-Rodríguez, J.M. Cabrera-Marrero, and J.J. Olaya-Florez: *Theor. Appl. Fract. Mech.*, 2016, vol. 86, pp. 351–60.
70. L. Morales-Rivas: *Metals (Basel)*, 2022, vol. 12, p. 195.